In-Plane Second-Order Topologically Protected States in Elastic Kagome Lattices

Qian Wu, Hui Chen, Xiaopeng Li, and Guoliang Huang*
Department of Mechanical and Aerospace Engineering, University of Missouri, Columbia, Missouri 65211, USA

(Received 17 February 2020; revised 8 May 2020; accepted 24 June 2020; published 28 July 2020)

Second-order topological insulators, which exhibit capability of hosting topologically protected zero-dimensional corner states distinct from the well-studied topological edge states, unveil a horizon beyond the conventional bulk-edge correspondence. Motivated by recent experimental observation of Wannier-type second-order corner states in acoustic structures, we investigate numerically and demonstrate experimentally the in-plane edge and corner states in a mechanical kagome lattice. By manipulating simply lattice geometry and quantized characterization, we exploit that the emerging corner states are topologically robust against disorders. We further present a second-order topological insulator with multi-interfaces such that the mechanical energy can be localized in multiple locations, which provides the possibility of practical application in energy harvesting devices. The present study is the physical observation to extend the second-order topological insulator to in-plane elastic dynamics, and modal coupling of in-plane elasticity makes it more challenging to be measured experimentally.

DOI: 10.1103/PhysRevApplied.14.014084

I. INTRODUCTION

As a fascinating platform for one-way robust wave propagation and signal transport, topological insulators (TIs) have been widely investigated in electronic [1–7], photonic [8–16], and phononic [17–22] systems. In general, TIs feature insulating bulk and conducting polarized edges. The conducting edges manifest as edge states, which mostly localize at boundaries and inhibit backscattering from boundary imperfection. Their topological features, including unidirectional conduction and robustness, pave the way for practical applications in areas of quantum computing [23] and lasing [24,25]. Other than their electronic predecessor, photonic and phononic TIs accompanied by quantum Hall effect were realized with time-reversal symmetry breaking [26–32]. After that, other topological phases, i.e., quantum valley Hall effect [33–46] and quantum spin Hall effect [47–51], were developed in time-reversal-invariant photonic and phononic systems. The bulk topology is generally classified by a topological invariant named Chern number, pinned to the bulk band gap [2]. With a nonzero topological invariant, the corresponding band gap is nontrivial, and hosts topological edge states exhibiting exceptional robustness against imperfections over a frequency range as long as the band gap remains open.

More recently, higher-order TIs (HOTIs) were theoretically achieved by gapping the edge states [52–57]. They belong to a special class of TIs where the conventional bulk-edge correspondence fails to apply. In general, a dth order TI hosts gapless protected edge states at $(h-d)$-dimensional boundaries enclosing the hth-dimensional bulk, where h must be greater than or equal to d [58]. Following this definition, in a 2D HOTI, gapless states are unavailable at (2–1)-dimensional (or 1D) boundaries, which suggests the presence of topologically unprotected first-order edge states. While second-order corner states confined at (2–2)-dimensional (or 0D) boundaries (corners) occur and are topologically protected. So far, the HOTIs can be classified into two categories, with one being quadruple type and the other being Wannier type. In 2018, the experimental realizations of microwave [59] and mechanical [60] HOTIs were reported in 2D electrical-circuit and mechanical square lattices, respectively, based on the quantization of quadrupole moments. Inspired by that, follow-up works demonstrated phononic Wannier-type HOTIs possessing C_3 and C_6 symmetries in 2D acoustic systems [58,61]. In these nonquadruple systems, Wannier center, serving as an alternative topological index, replaces the conventional topological variant, namely Chern number in conventional TIs, to interpret and predict the emergence of topological corner states. Checking the mismatch between the lattice sites and the Wannier centers is the primary criterion on determining whether the lattice is trivial or nontrivial. In such a manner, any 2D HOTI that follows the Wannier center interpretation can also be defined as a Wannier-type second-order topological insulator (SOTI). Aside from the 2D SOTIs, the third-order TI was recently experimentally demonstrated in a 3D acoustic diamond lattice [62]. It represents an extension of the acoustic Wannier-type SOTI. Recently, an experimental work reported on the realization of out-of-plane elastic SOTIs, carrying topological indices defined by the count

*huangg@missouri.edu

 © 2020 American Physical Society

of total topological charges at corners [63]. As of now the phononic Wannier-type SOTIs were only demonstrated in acoustic systems. The elastic in-plane Wannier-type SOTIs hence still remain to be realized.

In this paper, we make our attempt on the in-plane dynamics of thin mechanical lattice in plane-stress condition. We study numerically an elastic kagome lattice to achieve the in-plane Wannier-type SOTI through band structure and Wannier center engineering. The lattice configuration is characterized by extreme geometric simplicity, which makes it easy to manufacture using conventional laser-cutting or printing techniques. We then carry out experiments to validate our numerical prediction. We experimentally observe the in-plane second-order topological corner states, as well as the gapped edge states, in our elastic Wannier-type SOTI. Both numerical and experimental results suggest that the elastic SOTI can be characterized by the quantization of Wannier centers. Moreover, we leverage this platform by assembling sublattices with multi-interfaces. Both simulation and experiments reveal the coexistence of interface states and corner states in the sublattice system, implying potential applications in flexible energy storage and sensing.

II. DESIGN OF SOTI THROUGH BAND STRUCTURE AND WANNIER CENTER ENGINEERING

We start with an unperturbed unit cell of an elastic kagome lattice made of stainless steel ($\rho = 7850$ kg/m^3, $\nu = 0.28$, and $E = 209$ GPa), as illustrated in the middle panel of Fig. 1(a). It consists of three thin disks of equal radius r interconnected by bars of equal length, which perform as intracouplings and intercouplings. The widths of intrabars and interbars are denoted by w_1 and w_2 respectively, with the lattice constant and the thickness of the lattice being $a = 80$ mm and $b = 1.5$ mm, respectively. In general, the governing equation of the bulk elastic wave propagation in three-dimensional elastic media can be written as

$$\rho(\mathbf{r})\ddot{\mathbf{u}} = \nabla\{[\lambda(\mathbf{r}) + 2\mu(\mathbf{r})]\nabla\cdot\mathbf{u}\} - \nabla\times[\mu(\mathbf{r})\nabla\times\mathbf{u}], \tag{1}$$

where $\mathbf{u} = (u_x, u_y, u_z)$ denotes the displacement vector and $\lambda = E\nu/[(1+\nu)(1-2\nu)]$ and $\mu = E/[2(1+\nu)]$ represent the relationship between Lame's constants and Young's modulus E and Poisson's ratio ν. It is noteworthy that the proposed lattice consisting of the unit cells is designed to be a thin plate ($b \ll a$) such that the in-plane and out-of-plane motions can be decoupled. In other words, the equations governing the in-plane motion can be

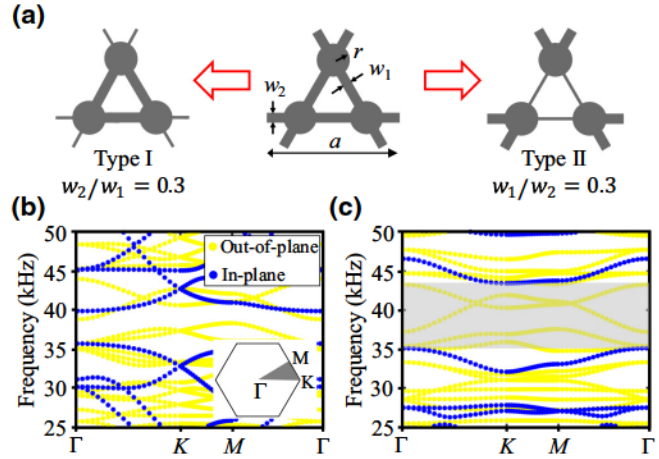

FIG. 1. Unit cells of kagome lattices and their band structures. (a) Schematic illustration of the unperturbed unit cell ($w_1 = w_2$) to type-I ($w_2/w_1 = 0.3$) and type-II ($w_1/w_2 = 0.3$) unit cells by breaking space-inversion symmetry. (b) Band structure of the unperturbed lattice. (c) Band structure of type-I and type-II lattices with a gray shaded area denoting the band gap of interest in this paper. In (b),(c), the blue dotted curves correspond to the in-plane motions whereas the yellow ones indicate the out-of-plane motions.

separated from Eq. (1) as

$$\rho(\mathbf{r})\omega^2 u_x + \frac{\partial}{\partial x}\left[(\lambda+2\mu)\frac{\partial u_x}{\partial x} + \lambda\frac{\partial u_y}{\partial y}\right] + \frac{\partial}{\partial y}\left[\mu\left(\frac{\partial u_x}{\partial y} + \frac{\partial u_y}{\partial x}\right)\right] = 0, \tag{2}$$

$$\rho(\mathbf{r})\omega^2 u_y + \frac{\partial}{\partial y}\left[(\lambda+2\mu)\frac{\partial u_y}{\partial y} + \lambda\frac{\partial u_x}{\partial x}\right] + \frac{\partial}{\partial x}\left[\mu\left(\frac{\partial u_y}{\partial x} + \frac{\partial u_x}{\partial y}\right)\right] = 0. \tag{3}$$

Based on the Bloch-Floquet theorem, the displacement vector in a periodic medium reads

$$\mathbf{u}(\mathbf{r}, t) = \mathbf{u}_\mathbf{k}(\mathbf{r})e^{i(\mathbf{k}\cdot\mathbf{r}-\omega t)}, \tag{4}$$

where $\mathbf{u}_\mathbf{k}(\mathbf{r})$ is the mode amplitude with $\mathbf{k} = (k_x, k_y)$. Substituting Eq. (4) into Eqs. (2) and (3) in the context of the finite-element method (FEM) and applying Floquet periodic boundary conditions leads to the following eigenvalue problem:

$$[\mathbf{K}(\mathbf{k}) - \omega^2\mathbf{M}]\mathbf{u}_\mathbf{k} = 0 \tag{5}$$

in which $\mathbf{K}(\mathbf{k})$ and $\mathbf{M}$ are the stiffness and the mass matrices, respectively. By sweeping $\mathbf{k}$ along the boundary of the first Brillouin zone, the band structure of the lattice can

be obtained by numerically solving Eq. (5). Figure 1(b) shows the band structure obtained numerically using the FEM-based package COMSOL Multiphysics for the case of the unperturbed lattice, where the widths of intrabars and interbars are chosen as $w_1 = w_2 = 6$ mm. We define the polarization coefficient of band n at $\mathbf{k}$ as $\alpha^{(n)}(\mathbf{k}) = \iiint_{\text{unitcell}} |u_z^{(n)}(\mathbf{k})|^2/[|u_x^{(n)}(\mathbf{k})|^2 + |u_y^{(n)}(\mathbf{k})|^2 + |u_z^{(n)}(\mathbf{k})|^2]\,dV$ such that the in-plane modes with $\alpha^{(n)}(\mathbf{k}) < 0.03$, indicated in blue, and the out-of-plane ones with $\alpha^{(n)}(\mathbf{k}) > 0.97$, indicated in yellow, can be evidently separated in the band structure. The in-plane Dirac cones are formed at K point due to the fact that C_{3v} symmetry is preserved in the unperturbed lattice. Slightly detuning the values of w_1 and w_2, i.e., the intercouplings and intracouplings, may give rise to gapless edge states by breaking the space-inversion symmetry. Their bulk topology can be characterized by a topological invariant called Chern number, and they are topologically protected against defects, sharp corners, and random disorders at nontrivial boundaries, corresponding to a mechanical analog of quantum valley Hall insulator (QVHI) for in-plane motions [43,46].

The SOTI can be accessed by detuning the intracouplings and intercouplings between sites, in a similar fashion of realizing mechanical QVHIs. In realizing the mechanical QVHI, a weak perturbation in the two types of couplings is required to open a band gap about the high symmetry points based on the conventional bulk-edge correspondence. It can be explained by Berry curvature, which determines the bulk topology of the lattice and can be quantitatively determined. A high concentration of Berry curvature at valleys secures the robustness of the mechanical QVHI as it gives a quantized Chern number. As the perturbation between the two couplings is gradually increased, the band gap becomes wider. This weakens the QVHI effect in consequence of Berry curvature fading away, and eventually leads the conventional bulk-edge correspondence to be inapplicable [44,45]. Instead of QVHI, higher-order topological corner states, which appear to be topologically robust, may exist within the wider band gap and its nontrivial bulk topology can be characterized by quantized Wannier centers [54,55], expressed as

$$P_i = -\frac{1}{S}\iint_{\text{BZ}} A_i(\mathbf{k})\,d^2\mathbf{k}, \quad i = x, y, \tag{6}$$

where S denotes the area of the first Brillouin zone, and $A_i(\mathbf{k}) = -\text{Im}[u_x^*(\mathbf{k},\mathbf{r})\mathbf{M}\partial_{k_i}u_x(\mathbf{k},\mathbf{r}) + u_y^*(\mathbf{k},\mathbf{r})\mathbf{M}\partial_{k_i}u_y(\mathbf{k},\mathbf{r})]$ is the Berry connection with $\mathbf{u} = (u_x, u_y)$ being the normalized eigenmodes extracted from numerical simulation [22,50].

In order to investigate the possible corner state in our proposed kagome lattice, we enlarge the deviation between the intercouplings and intracouplings by shrinking one of w_1 and w_2 down to 1.8 mm while keeping the other unaltered. The reason we select this value is due to the fact that

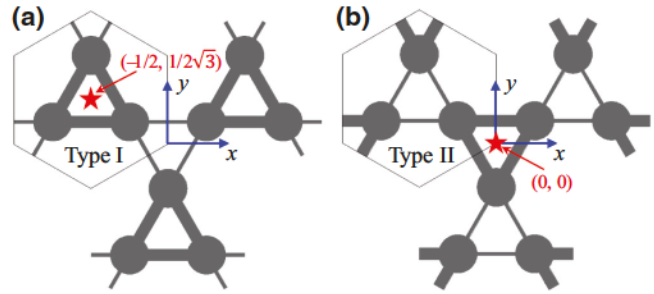

FIG. 2. Determination of the Wannier centers. (a) Wannier center for type-I unit cell that is located at the center of the unit cell denoted by the red stars. (b) Wannier center for type-II unit cell that is located at the origin of coordinates.

it leads to the birth of in-gap higher-order corner states. This is further discussed in the following section and in Fig. 7 in Appendix A. Two distinct unit cells (named type I and type II) are shown in the left and right panels of Fig. 1(a), respectively. They possess identical band structures; see Fig. 1(c). A large omnidirectional band gap, indicated by a shaded area and centered about 40 kHz, can be observed, spanning about 9 kHz and making the bulk insulating for in-plane motions. As can be seen from Fig. 2(a), the type-I unit cell ($w_2/w_1 = 0.3$) holds its Wannier center at its center $(-1/2, 1/2\sqrt{3})$. For the type-II unit cell ($w_1/w_2 = 0.3$), the Wannier center lies at the origin $(0, 0)$, i.e., the center of the downward-pointing triangle; see Fig. 2(b). As has been pointed out in previous studies [54,55,58,61]: if a finite structure cuts along the Wannier centers, it is nontrivial and the presence of the second-order corners states can be expected at the corner as well as the topological edge states at the boundary, which is numerically and experimentally demonstrated in the following section.

To further demonstrate the existence of edge states as well as corner states, we construct two types of supercells with type-I and type-II unit cells. In the simulation, the supercell is composed of a 12×1 array of unit cells and is terminated by a free boundary along the x direction and Floquet-Bloch boundary conditions along the y direction. Figures 3(a) and 3(b) show the band structures of supercells with type-I and type-II unit cells, respectively. The blue dots represent the in-plane states while the yellow dots represent the out-of-plane ones. For the supercell with type-I unit cells, no in-plane edge states exist in the band gap, suggesting that the resultant lattice is topologically trivial; see Fig. 3(a). While for the supercell with type-II unit cells, there are indeed three in-plane edge states in the band gap, indicating the lattice formed by type-II unit cells is topologically nontrivial. This can be well explained by Wannier centers since the boundary of the supercell with type-I unit cells do not cut through the Wannier center but the supercell with type-II unit cells do. In Fig. 3(c),

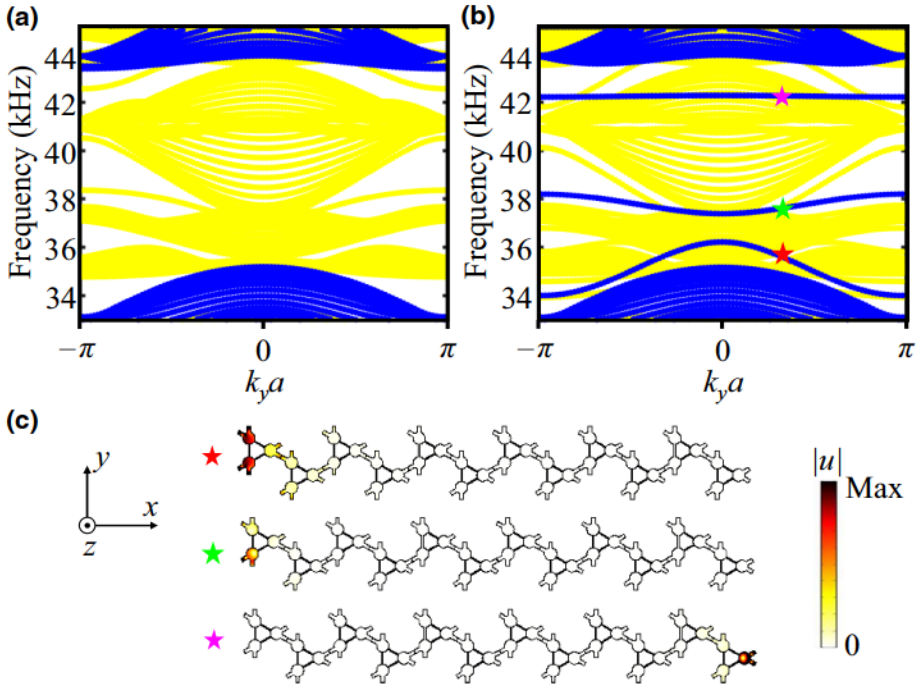

FIG. 3. Band structures of supercells. (a) Numerically attained band structure of the supercell consisting of 12×1 type-I unit cells. (b) Numerically attained band structure of the supercell consisting of 12×1 type-II unit cells. Within the band gap, three in-gap gapped edge states appear, and their displacement field profiles at $k_y a = 0.3\pi$ are displayed in (c). In (a),(b), the blue dotted curves correspond to the in-plane motions whereas the yellow ones indicate the out-of-plane motions.

the states highlighted by red and green stars represent the left edge states. In general, existence of gapped edge states may lead to the emergence of second-order corner states, which do not propagate and are highly localized at the corner with topological protection. As shown in Fig. 3(b), the state highlighted by magenta stars at 42.27 kHz possesses a flat band dispersion, and hence has a zero group velocity, which makes it highly localized at boundary segment. It ensures the presence of high-order corner states in our proposed kagome lattice.

III. NUMERICAL AND EXPERIMENTAL OBSERVATION OF SOTI

To investigate the possible in-plane second-order corner states in the elastic kagome lattice, numerical modal analysis is conducted using COMSOL Multiphysics. A 5×5 parallelogram-shaped lattice enclosed by trivial and nontrivial edges is illustrated in Fig. 4(a). For such a lattice, additional simulations are performed to check the dependence of the emergence of corner states on the ratio of two couplingsw_1/w_2 (see Fig. 7 in Appendix A). When the ratio w_1/w_2 takes a value between 0.2 and 0.4, the topological corner state can be found in the band gap. The numerically calculated eigenfrequency spectrum presented in Fig. 4(b) shows that a series of in-plane edge states and an in-plane corner state are within the band gap (shaded area). Their corresponding mode shapes are shown in Figs. 4(c)–4(e). Figure 4(c) illustrates the in-plane displacement distributions of bulk states at 34.8 kHz. As can be seen from Figs. 4(d) and 4(e), edge modes at 38.15 kHz and a top-right corner state at 42.4 kHz are respectively localized on the nontrivial boundaries and nontrivial corners, which are terminated by Wannier centers. In contrast, the trivial ones (denoted by green dashed lines) cannot support any topologically protected edge and corner states, since the Wannier centers are not localized at the upward-pointing triangles. Furthermore, we introduce disorders by perturbing the radii of all the sites except the bottom-left three corners [see Fig. 8(a) in Appendix B]. The calculated frequency spectrum in Fig. 8(b) shows the topological corner state remains pinned to the same frequency with varied thickness ratio, which verifies the robustness of the corner states against the disorders.

To experimentally demonstrate the topologically protected corner state as well as the edge states, we fabricate an elastic kagome lattice made of stainless steel by using a laser-cutting technique. The experimental setup is shown in Fig. 5(a), and a schematic illustration with more details is given in Appendix C. We first excite the in-plane motion with piezoelectric (PZT) patch source and measure the time-domain signal at the four points [denoted by A, B, C, and D in the inset of Fig. 5(a)]. In order to excite the nonpropagating corner state, the source is placed only half a lattice constant away from the predicted nontrivial corner. Although the source is not exactly located at the corner, the corner state is still expected to be excited efficiently due to the region of overlap between the source field and the nonzero decaying field of the corner state. Specifically, point A is at the corner at which the previous numerical results predict the existence of the corner state. In order to monitor the edge and bulk states, points B and C are assigned at the two nontrivial edges, while

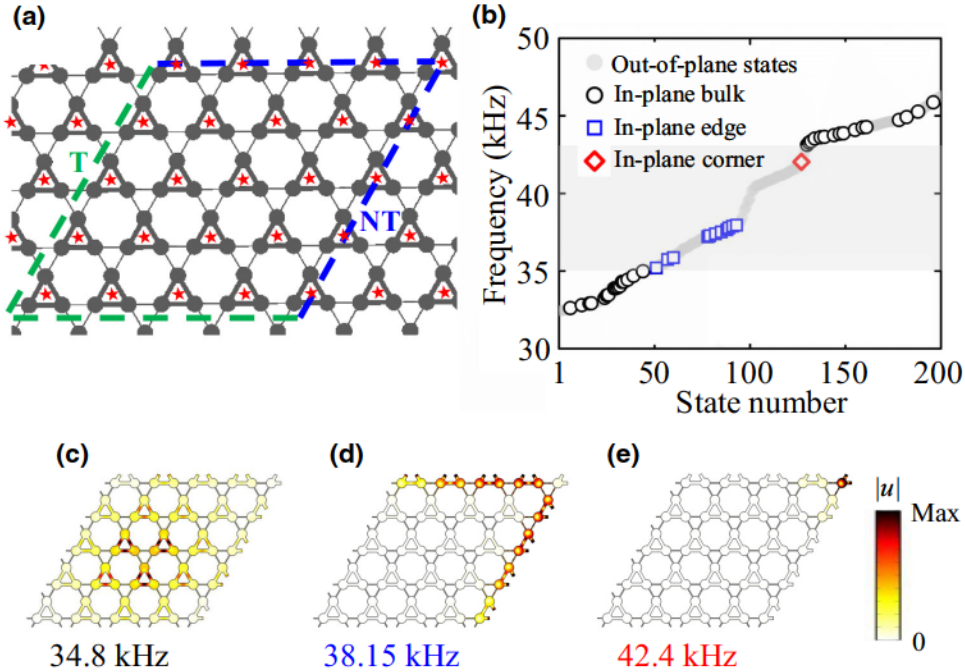

FIG. 4. Numerical results from the eigenstate analysis of a 5 × 5 lattice. (a) Schematic illustration of the finite lattice. The red stars indicate the Wannier center positions. "NT" with blue dashed lines represents the nontrivial edges, which support localized states, whereas "T" with green ones corresponds to the trivial edges where no localized state exists. (b) Numerically calculated eigenfrequency spectrum with shaded area representing the bulk band gap of interest. The corresponding mode shapes are listed: (c) bulk state at 34.8 kHz, (d) edge state at 38.15 kHz, (e) corner state at 42.4 kHz.

point D is in the bulk. The energy spectrum is obtained by applying the Fourier transform to the time-domain signals collected at the four points. Figure 5(b) shows the measured normalized energy [also called frequency-domain power density $|P_x|^2 + |P_y|^2$, where P_x and P_y represent the power-spectrum densities (PSD) of velocity fields along x and y direction, respectively] with a ten-cycle tone burst excitation centered at 36 kHz [see Fig. 9(b) in Appendix C]. The signal interval is set to be 3 s for all burst signals used in the rest of the paper. Multiple peaks around 37 kHz can be visualized. The intensity at point A is quite low when compared to those at the other points at the edges. While the peaks at point D only suggests the presence of the bulk states. These results confirm the

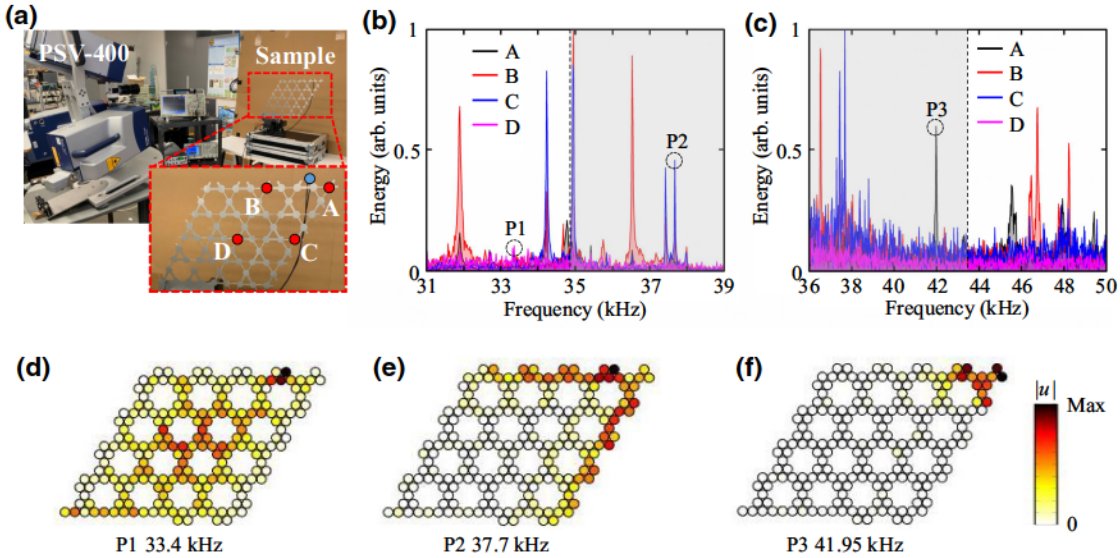

FIG. 5. Experimental observation of topological states in a 5 × 5 kagome lattice. (a) Photograph of the experimental setup. The normalized energy spectra from the excitation of two ten-cycle tone burst signals centered at (b) 36 kHz and (c) 42 kHz are retrieved through Fourier transformation. The energy coefficient in each figure is normalized to its own maximum value. There are three highlighted frequencies, P1, P2, and P3, representing bulk, edge, and corner states, respectively. Note the shaded areas in (b),(c) indicate the numerically determined band gap. The experimentally measured mode shapes of the three frequencies are illustrated: (c) bulk state at 33.4 kHz, (d) edge state at 37.7 kHz, (e) corner state at 41.95 kHz.

existence of the edge states at the two nontrivial edges. We then conduct full field measurements at 33.4 kHz (P1) and 37.7 kHz (P2) by exciting the lattice with a 200-cycle sine burst. The corresponding measured energy distributions at these two frequencies are shown in Figs. 5(d) and 5(e). For the bulk state, the energy spreads in the bulk, while for the edge state, the energy is localized along the edges and decays toward the bulk. For a better observation of the corner state, we switch to another tone burst excitation whose center frequency is now set as 42 kHz [see Fig. 9(c) in Appendix C]. As can be seen from Fig. 5(c), extremely strong response is gathered at 41.95 kHz at point A, while nothing but background noise is recorded at the other three points. It indicates the existence of the corner state. By sweeping for the in-plane velocity distribution at 41.95 kHz (P3), we can clearly witness from Fig. 5(f) that the corner state associated with strong energy localization at the top-right corner formed by the two nontrivial edges. The energy does not spread, which is quite distinct from the cases of the bulk and edge states. All the experimentally measured bulk, edge, and corner states exhibit great agreement with the numerical ones shown in Figs. 4(c)–4(e). Minor shifts of the experimental measurements from the numerical results are due to the existence of some fabrication errors and the discrepancies in material parameters. To confirm the absence of the edge and the topological corner states in a trivial 5×5 lattice, a comparison between the trivial and the nontrivial lattices is made through performing numerical transient simulations (see Appendix D).

Lastly, we construct another parallelogram-shaped kagome lattice that contains four sublattices, as illustrated in Fig. 6(a). The purpose of this study is to reveal a possible application that the proposed in-plane Wannier-type SOTI allows the in-plane energy localization and storage at multiple locations with topologically protected edge and corner states. This may lead to a realization of flexible energy harvesting devices. In the design, two of the sublattices covered by the gray areas are composed of type-II unit cells whereas the others consist of type-I unit cells. They are separated by four interfaces. Two of the interfaces highlighted by blue dashed lines are constructed with bars of larger width ($w_2 > w_1$), while the other in green are formed by connecting the two distinct lattices with thinner bars($w_1 < w_2$) [see Fig. 6(a)]. The numerically calculated eigenfrequency spectrum of this lattice, shown in Appendix E, reveals the existence of localized in-plane states within the band gap. To experimentally verify the existence of the localized states, we excite the in-plane motion through a PZT source [blue point in Fig. 6(a)] with a tone burst signal centered at 40 kHz, and measure the time-domain response at six points. After Fourier transform, the normalized frequency-domain energy spectra for the six points between 33 and 37 kHz are retrieved and shown in Fig. 6(b). From the measurement, energy

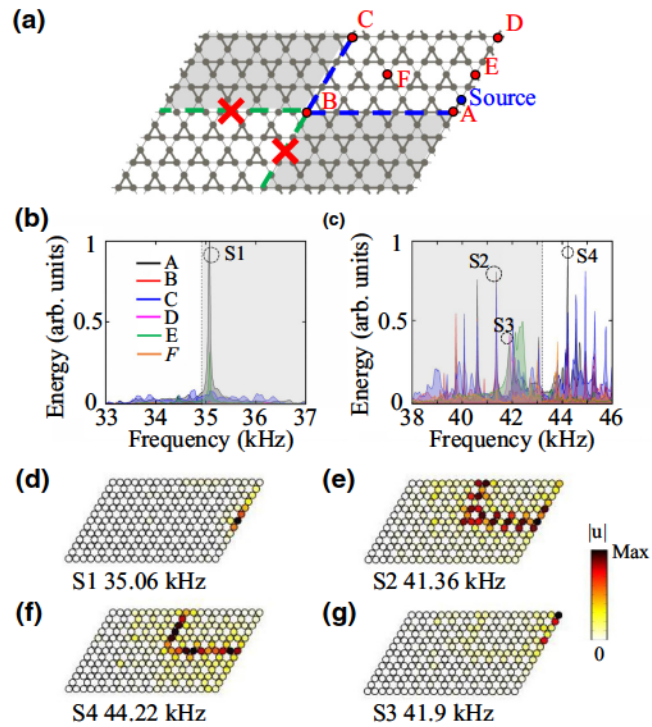

FIG. 6. Experimental observation of topological states in a kagome lattice containing four sublattices. (a) Schematic illustration of the proposed lattice containing four sublattices. Two sublattices are made of type-I unit cells (top right and bottom left), and the other two are composed of type-II unit cells (top left and bottom right). Two classes of interfaces are highlighted in green dashed and blue dashed lines, respectively. Note that the interfaces in blue can support gapped in-plane interface states whereas the ones in green cannot. Retrieved energy spectra from the measured time-domain responses by a tone burst excitation at 40 kHz are displayed separately within two regions: (b) 33 to 37 kHz, (c) 38 to 46 kHz. Both of them are normalized to their own maximum values. Note the shaded areas in (b),(c) indicate the numerically determined band gap. Four peaks, S1, S2, S3, and S4, are selected to demonstrate the localized in-plane states: (d) trivial corner state at 35.06 kHz, (e) interface state at 41.36 kHz, (f) interface state at 44.22 kHz, (g) topological corner state at 41.9 kHz, respectively.

peaks with extremely strong intensities show up around 35.06 kHz (S1) only at points A and G while only noise is recorded at other tested points. This suggests the excitation of the trivial corner states, which have been numerically investigated in Appendix E. Then, we send a 200-cycle sine burst signal of 35.06 kHz to inspect the intensity distribution. As shown in Fig. 6(d), strong energy concentration is observed at the trivial corner (point A) formed by the trivial and nontrivial edges and the interfaces. In addition, nonzero energy confinement can be found at the other trivial corner (point C), although the intensity turns out to be much weaker than that of point A due to the fact that point A locates much closer to the excitation PZTs. Note that there is nonzero field intensity residing along

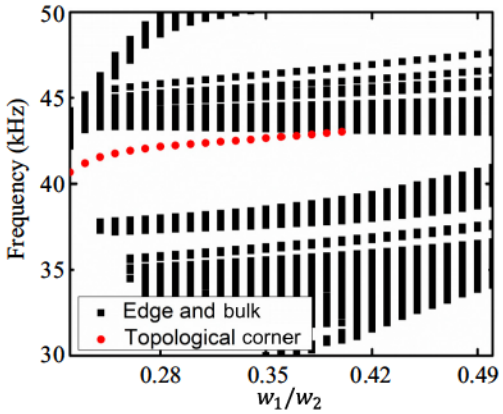

FIG. 7. Frequency spectrum for a parallelogram-shaped lattice with varied width ratio, w_1/w_2. Red dots represent corner states and black dots represent edge and bulk states.

the nontrivial edges. This is due to the fact that the trivial corner states are within the region of trivial edge states as can be seen in Appendix E. The employed sine burst signal having an interval of 3 s actually contains nonzero energy components on frequencies other than the center frequency (36.05 kHz). The excited trivial edge states of less interest may inevitably but quite slightly contaminate the energy spectra of trivial corner states. Moreover, the normalized energy spectra ranging from 38 to 46 kHz are shown in Fig. 6(c). Multiple peaks are visualized at points A, B, and C. They are within the two interface state regions shown in Appendix E. By switching to 200-cycle sine burst excitation at 41.36 (S2) and 44.22 kHz (S4), we find that the two highlighted peaks indeed correspond to interface states possessing great energy localization along the interfaces, as shown in Figs. 6(e) and 6(f). In addition, we find nothing but only one peak at point D at 41.9 kHz (S3), which reveals the occurrence of the topological corner state. The energy distribution for this state is given in Fig. 6(g). Strong energy localization can be found at the nontrivial corner, similarly to what we have seen in Fig. 4(e). In addition to the corner state, interface states with significantly weaker magnitudes is also visible. This can be well explained as the excitation of the interface states by the nonzero noncentered frequencies, since the topological corner state lies within the interface state band [see Fig. 11(a) in Appendix E]. The experimental results slightly deviate with respect to the numerical ones. We believe this results from some minor discrepancies in material parameters and the slight lattice bending by self gravity. In both experiments, we intentionally add additional support plates to fix the samples. Additional numerical modal analysis of the two lattices in the presence of the support plates are conducted (see Fig. 12 in Appendix F). The calculated eigenfrequency spectra indicate that the support plates only introduce extra bulk states of less interest, and barely affect the spectral locations and the occurrence of edge and corner states.

IV. CONCLUSION

In this work, we study numerically and demonstrate experimentally the in-plane dynamics of Wannier-type SOTI in elastic kagome lattices with bivalued widths of bars that breaks the space-inversion symmetry. First, we design a simple kagome lattice to show the topologically protected corner states, lying in the nontrivial band gap, can robustly concentrate the wave energy at Wannier centers. Apart from the conventional bulk-edge correspondence, the Wannier center provides an additional degree of freedom to toggle on and off the topological corner state. Based on this principle, we further design a larger kagome lattice with multi-interfaces and use them to realize a device that can harvest and store energy in multiple locations. The present study extends the applicability of the SOTI to in-plane elastic dynamics in the experiment, and enrich the understanding of topological phenomena in the mechanical metamaterials. Our work may lead to applications of mechanical metamaterials in local elastic field enhancement, trapping and manipulating of elastic waves, elastic sensing, and probing.

ACKNOWLEDGMENTS

This work is supported by the Air Force Office of Scientific Research under Grant No. AF 9550-18-1-0342

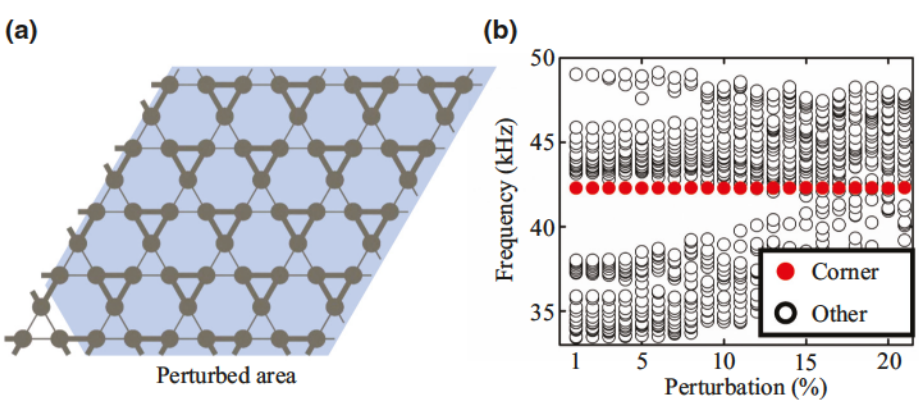

FIG. 8. Robustness of the topological corner states. (a) Parallelogram-shaped lattice under disordered radii of the sites except the bottom-left three corners. The disordered area is highlighted by the blue color. (b) Frequency spectrum with different disorder strengths. Red dots represent corner states and black dots represent edge and bulk states.

with Program Manager Dr. Byung-Lip (Les) Lee, the NSF EFRI under Award No. 1641078 and the Army Research Office under Grant No. W911NF-18-1-0031 with Program Manager Dr. Daniel Cole.

Q.W. and H.C. contributed equally to this work.

APPENDIX A: TOPOLOGICAL CORNER STATES

By tuning the ratio of width between the intrabars and interbars, one can toggle the occurrence of the topological corner state. Here we consider a parallelogram-shaped lattice in Fig. 4(a) of the main text. In Fig. 7, we calculate the eigenfrequency spectrum under different ratio, w_1/w_2. It is found that the corner states exist at the top-right corner when $0.2 < w_1/w_2 < 0.4$. Thus, in the main text, we choose $w_1/w_2 = 0.3$ in the design of SOTI as this allows the corner state to appear within the band gap.

APPENDIX B: ROBUSTNESS OF CORNER STATES

In this section, we perform an eigenfrequency study on the robustness of the corner states against disorders based on the numerical simulation. As shown in Fig.

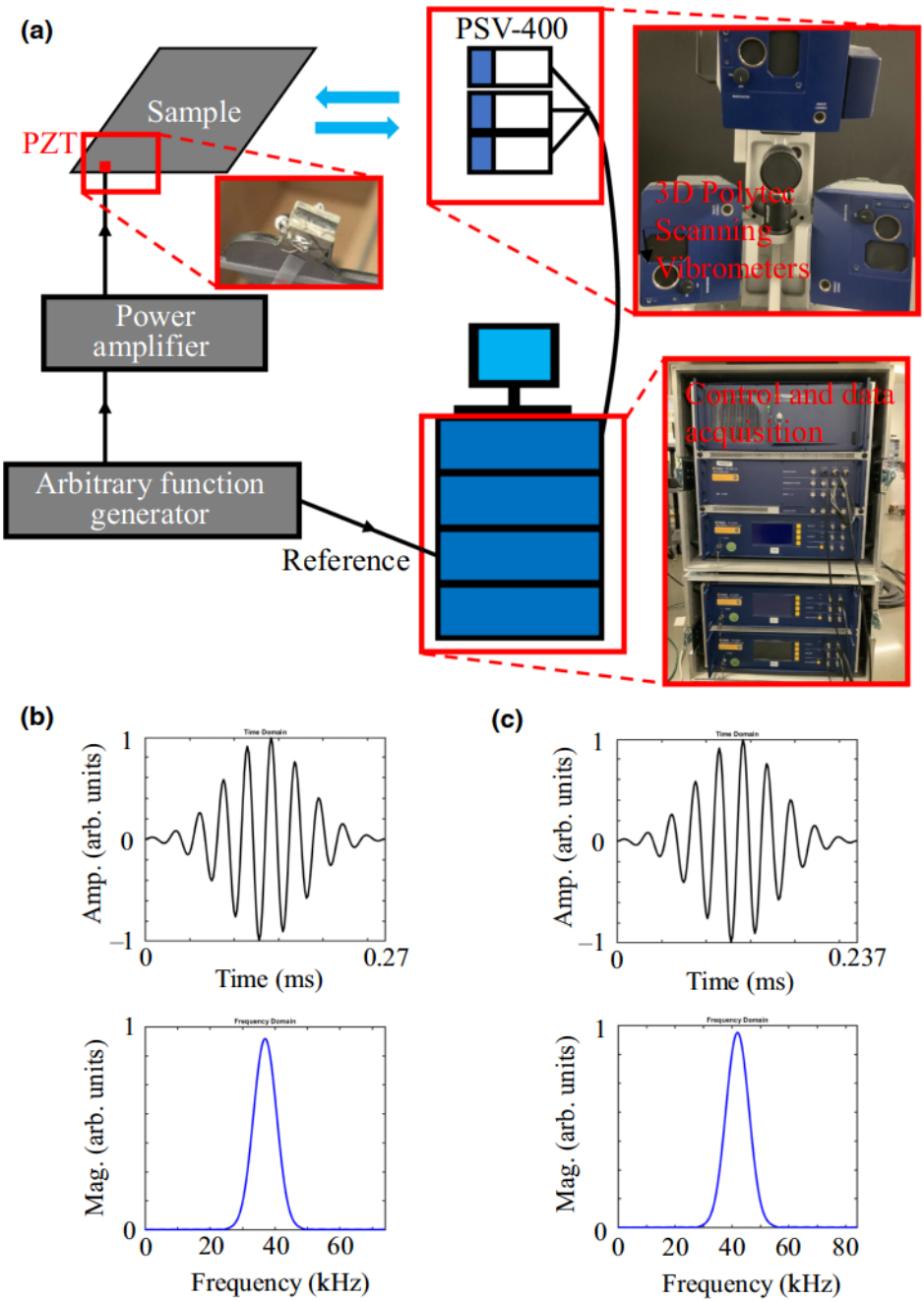

FIG. 9. (a) Schematic illustration of the experimental setup. Two excitation signals and their frequency spectra centered at (b) 36 kHz and (c) 42 kHz, respectively.

8(a), we allow the radii of sites in the highlighted area of the parallelogram-shaped lattice to be randomly displaced by δr with respect to their original radii r. The disorder strength is defined as $100\% \times \max(\delta r)/r$. Here the disorder parameters are generated by the random function in MATLAB script. Note that radii of the bottom-left three disks remain unaltered. As can be clearly seen from Fig. 8(b), the frequency of the topological corner state remains pinned to the same frequency with different disorder strength. Such insensitivity to the disorder of corner states suggests possible applications for sensing where the mode can be well confined.

APPENDIX C: EXPERIMENTAL SETUP AND PLATE CONFIGURATIONS

Figure 9(a) shows the experimental setup. The in-plane velocity wave field is accurately measured by a 3D scanning laser Doppler vibrometer (SLDV, Polytech PSV-400). To produce the in-plane motion in the sample, tone burst signals [Figs. 9(b) and 9(c)] are generated by a Tektronix AFG3022C arbitrary waveform generator and amplified by a Krohn-Hite high-voltage power amplifier, which is finally applied across the double-sided PZT-5H source. The velocity signal from the vibrometer is further recorded by the PSV-400 data acquisition. All the instruments are connected with the computer for real-time monitoring, automatic scanning, and signal processing.

The two experimental plates in Figs. 5(a) and 6(a) are fabricated by a fiber laser-cutting machine. Their structural parameters are the same as ones adopted in the numerical simulations, except for the presence of an additional thin rectangular support plate, which is fixed by the clamp. Since there is no energy confinement at trivial edges, it is safe to place the support plate over there such that it will

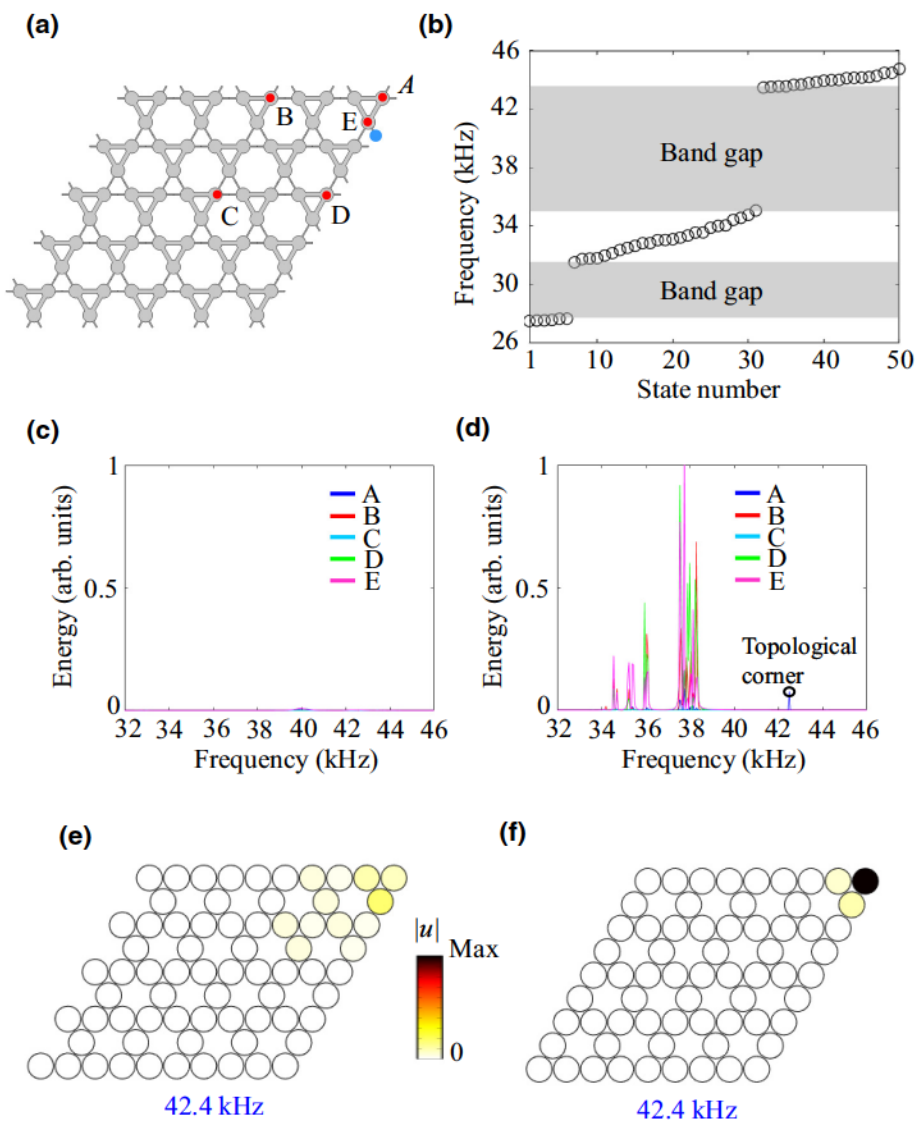

FIG. 10. Numerical transient analysis of trivial and nontrivial lattices. (a) Schematic illustration of the trivial lattice defined by trivial edges. The cyan point represents the location of the source in transient simulations, while the other five points are assigned for checking the possibility of topological corner state. (b) Numerically calculated eigenfrequency spectrum of the trivial lattice, with shaded area representing the bulk band gaps. (c),(d) Normalized energy spectra retrieved through Fourier transformation on the time-domain signals collected at the five highlighted points shown in (a) for the trivial and the nontrivial lattices, respectively. (e),(f) Normalized in-plane displacement fields measured at 42.4 kHz (topological corner state frequency) for the trivial and the nontrivial lattices, respectively. The tone burst signal is centered at 40 kHz and is sent in at the position highlighted in cyan in (a). The collecting points are chosen to be the disk centers.

not affect the topological states in the kagome lattice [see Figs. 12(c) and 12(d) in Appendix F].

APPENDIX D: NUMERICAL TRANSIENT ANALYSIS OF TRIVIAL AND NONTRIVIAL LATTICES

In order to graphically illustrate the difference between nontrivial and trivial lattices, a finite trivial lattice is constructed with type-I units in Fig. 10(a) and the eigenfrequency spectrum is calculated and plotted in Fig. 10(b). As can be seen in Fig. 10(b), no topological state (including edge and corner states) within the band gap of interest has been observed in the trivial lattice, which significantly differs from the nontrivial case in Fig. 4. Specifically, to further validate the lack of the topological corner state in this trivial lattice, we conduct transient numerical simulations to mimic experimental testing. In the simulation, the excitation involved is a tone burst signal centered at 40 kHz and placed at the cyan point shown in Fig. 10(a). The normalized energy spectra, present in Fig. 10(c), can be obtained by performing Fourier transformation of the time-domain signals collected at the five points highlighted in Fig. 10(a). For a clear comparison, the normalized energy spectra for the nontrivial lattice are calculated in Fig. 10(d). For the nontrivial lattice, extremely strong response is observed at 42.4 kHz at point A but nothing is recorded at the other four points, which is in good agreement with the experimental measurement present in Fig. 5. However, for the trivial lattice, no localized state can be visualized within the frequency range of interest. Last, the normalized in-plane displacement fields at 42.4 kHz for the trivial and the nontrivial lattices are plotted in Figs. 10(e) and 10(f), respectively. Strongly localized corner state can be graphically illustrated for the nontrivial lattice, whereas the trivial lattice cannot support this state.

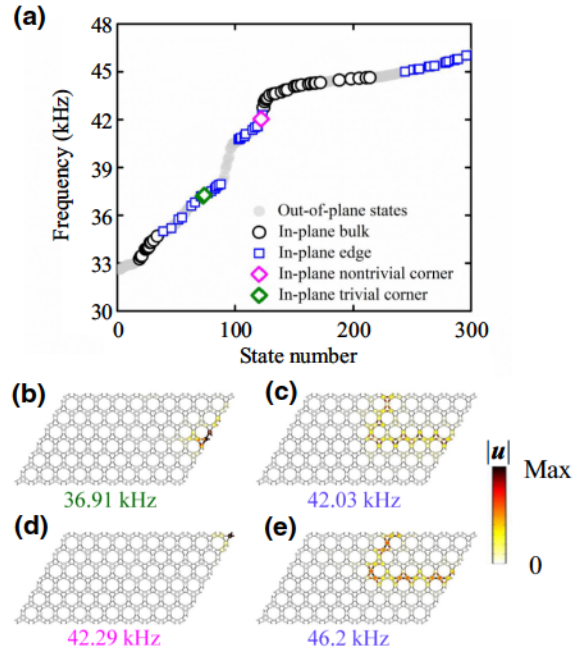

FIG. 11. Eigenmode simulations of a kagome lattice containing four sublattices shown in Fig. 6(a). (a) Numerically calculated eigenfrequency spectrum of the lattice. Numerically calculated mode shapes: (b) trivial corner state at 36.91 kHz, (c) interface state at 42.03 kHz, (d) topological corner state at 42.29 kHz, and (e) interface state at 46.2 kHz.

APPENDIX E: NUMERICAL RESULTS OF THE KAGOME LATTICE CONTAINING FOUR SUBLATTICES

There are two types of interfaces highlighted with the trivial ones highlighted in green dashed lines and the nontrivial one in blue dashed lines, as shown in Fig. 6(a). The kagome lattice is then divided into four parts. Among them two are formed by type-I unit cells while the others consist of type-II unit cells. The numerically calculated eigenfrequencies and eigenmodes are shown in Figs. 11(a) and 11(b)–11(e), respectively. As expected, one in-plane topological corner state is found at 42.29 kHz. Figure 11(d) illustrates the eigenmode of the topological corner state and shows it is highly localized at the top-right corner of the kagome lattice. The in-plane interface states are shown in Figs. 11(c) and 11(e). In addition, trivial corner states can be found around 36.91 kHz, as shown in Fig. 11(b). Unlike the topological one, they are not localized at the Wannier center, and hence are not topologically protected. All these numerical results are consistent with the experimental results shown in the main text.

APPENDIX F: INFLUENCE OF THE SUPPORT PLATE ON THE TOPOLOGICAL STATES

The support plates in the experimental samples shown in Figs. 12(a) and 12(b) are not considered in the numerical simulation in the main text. In this section, we conduct numerical eigenfrequency analysis of the experimental samples to demonstrate the support plates barely affect the occurrence of topological corner and edge states. Figures 12(c) and 12(d) indicate that the edge and corner states are almost unaltered when compared to the results shown in Figs. 4(b) and 11(a). This is due to the fact that the support plates are added onto the trivial boundaries, where no localized states exist, such that they cannot affect the nontrivial topological states.

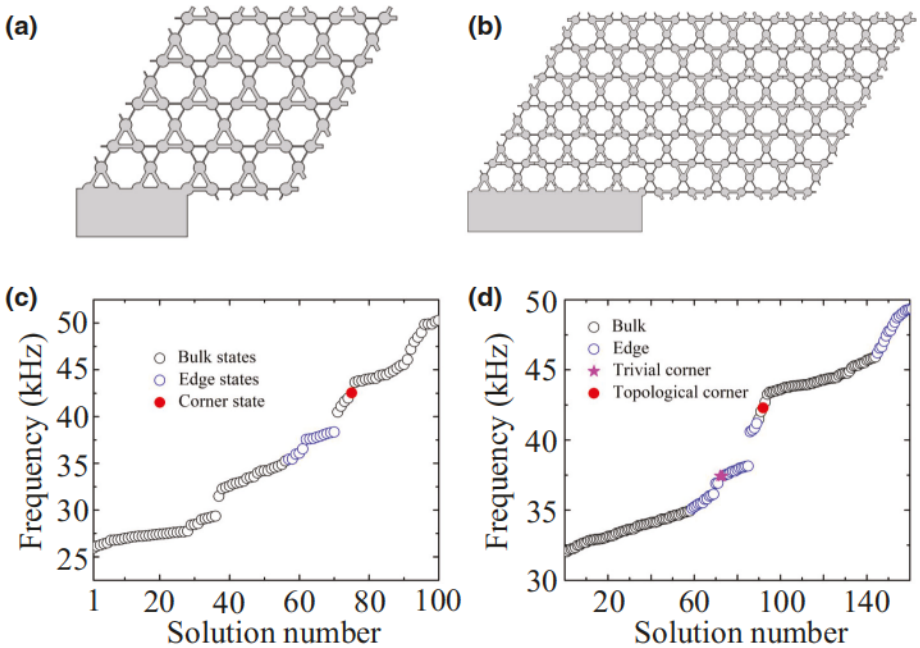

FIG. 12. Numerical eigenfrequency analysis of the experimental samples with support plates. Lattices (a),(b) are two samples measured in the experiments. (c),(d) are numerical frequency spectra of (a),(b), respectively.

[1] X. L. Qi and S. C. Zhang, Topological insulators and superconductors, Rev. Mod. Phys. **83**, 1057 (2011).

[2] M. Z. Hasan and C. L. Kane, Colloquium: Topological insulators, Rev. Mod. Phys. **82**, 3045 (2010).

[3] F. D. M. Haldane, Model for a QHE Without Landau Levels, Phys. Rev. Lett. **61**, 2015 (1988).

[4] C. L. Kane and E. J. Mele, Z_2 Topological Order and the Quantum Spin Hall Effect, Phys. Rev. Lett. **95**, 146802 (2005).

[5] C. L. Kane and E. J. Mele, Quantum Spin Hall Effect in Graphene, Phys. Rev. Lett. **95**, 226801 (2005).

[6] D. Xiao, W. Yao, and Q. Niu, Valley-Contrasting Physics in Graphene: Magnetic Moment and Topological Transport, Phys. Rev. Lett. **99**, 236809 (2007).

[7] F. D. M. Haldane and S. Raghu, Possible Realization of Directional Optical Waveguides in Photonic Crystals with Broken Time-Reversal Symmetry, Phys. Rev. Lett. **100**, 013904 (2005).

[8] M. Hafei, E. A. Demler, M. D. Lukin, and J. M. Taylor, Robust optical delay lines with topological protection, Nat. Phys. **7**, 907 (2011).

[9] A. B. Khanikaev, S. H. Mousavi, W. K. Tse, M. Kargarian, A. H. MacDonald, and G. Shvets, Photonic topological insulators, Nat. Mater. **12**, 233 (2013).

[10] A. B. Khanikaev and G. Shvets, Two-dimensional topological photonics, Nat. Photonics **11**, 763 (2017).

[11] D. Leykam, M. C. Rechtsman, and Y. D. Chong, Anomalous Topological Phases and Unpaired Dirac Cones in Photonic Floquet Topological Insulators, Phys. Rev. Lett. **117**, 013902 (2016).

[12] L. Lu, J. D. Joannopoulos, and M. Soljačić, Topological photonics, Nat. Photonics **8**, 821 (2014).

[13] T. Ozawa, H. M. Price, A. Amo, N. Goldman, M. Hafezi, L. Lu, M. C. Rechtsman, D. Schuster, J. Simon, O. Zilberberg, and I. Carusotto, Topological photonics, Rev. Mod. Phys. **91**, 015006 (2019).

[14] Y. Plotnik, M. C. Rechtsman, D. Song, M. Heinrich, J. M. Zeuner, S. Nolte, and M. Segev, Observation of unconventional edge states in 'photonic graphene', Nat. Mater. **13**, 57 (2014).

[15] M. C. Rechtsman, J. M. Zeuner, Y. Plotnik, Y. Lumer, D. Podolsky, F. Dreisow, and A. Szameit, Photonic Floquet topological insulators, Nature **496**, 196 (2013).

[16] S. A. Skirlo, L. Lu, and M. Soljačić, Experimental Observation of Large Chern Numbers in Photonic Crystals, Phys. Rev. Lett. **113**, 113904 (2014).

[17] V. Peano, C. Brendel, M. Schmidt, and F. Marquardt, Topological Phases of Sound and Light, Phys. Rev. X **5**, 031011 (2015).

[18] S. D. Huber, Topological mechanics, Nat. Phys. **12**, 621 (2016).

[19] R. Süsstrunk and S. D. Huber, Classification of topological phonons in linear mechanical metamaterials, Proc. Natl. Acad. Sci. U.S.A. **113**, E4767 (2016).

[20] M. Xiao, G. Ma, Z. Yang, P. Sheng, Z. Q. Zhang, and C. T. Chan, Geometric phase and band inversion in periodic acoustic systems, Nat. Phys. **11**, 240 (2015).

[21] S. Y. Huo, J. J. Chen, H. B. Huang, and G. L. Huang, Simultaneous multi-band valleyprotected topological edge states of shear vertical wave in twodimensional phononic crystals with veins, Sci. Rep. **7**, 10335 (2017).

[22] S. Y. Yu, C. He, Z. Wang, F. K. Liu, X. C. Sun, Z. Li, H. Z. Lu, M. H. Lu, X. P. Liu, and Y. F. Chen, Elastic pseudospin transport for integratable topological phononic circuits, Nat. Commun. **9**, 3072 (2018).

[23] A. Y. Kitaev, Unpaired majorana fermions in quantum wires, Physics-Uspekhi **171**, 131 (2000).

[24] G. Harari, M. A. Bandres, Y. Lumer, M. C. Rechtsman, Y. D. Chong, M. Khajavikhan, D. N. Christodoulides, and M. Segev, Topological insulator laser: Theory, Science **359**, eaar4003 (2018).

[25] M. A. Bandres, S. Wittek, G. Harari, M. Parto, J. H. Ren, M. Segev, D. N. Christodoulides, and M. Khajavikhan, Topological insulator laser: Experiments, Science **359**, eaar4005 (2018).

[26] S. A. Skirlo, L. Lu, Y. Igarashi, Q. Yan, J. D. Joannopoulos, and M. Soljačić, Experimental Observation of Large Chern Numbers in Photonic Crystals, Phys. Rev. Lett. **115**, 253901 (2015).

[27] Z. Wang, Y. Chong, J. D. Joannopoulos, and M. Soljačić, Observation of unidirectional backscattering-immune topological electromagnetic states, Nature **461**, 772 (2009).

[28] L. M. Nash, D. Kleckner, A. Read, V. Vitelli, A. M. Turner, and W. T. M. Irvine, Topological mechanics of gyroscopic metamaterials, Proc. Natl. Acad. Sci. U.S.A. **112**, 14495 (2015).

[29] E. Prodan and C. Prodan, Topological Phonon Modes and Their Role in Dynamic Instability of Microtubules, Phys. Rev. Lett. **103**, 248101 (2009).

[30] A. Souslov, B. C. van Zuiden, D. Bartolo, and V. Vitelli, Topological sound in active-liquid metamaterials, Nat. Phys. **13**, 1091 (2017).

[31] Z. Yang, F. Gao, X. Shi, X. Lin, Z. Gao, Y. Chong, and B. Zhang, Topological Acoustics, Phys. Rev. Lett. **114**, 114301 (2015).

[32] H. Chen, L. Y. Yao, H. Nassar, and G. L. Huang, Mechanical Quantum Hall Effect in Time-Modulated Elastic Materials, Phys. Rev. Appl. **11**, 044029 (2019).

[33] F. Gao, H. Yang, K. Lai, Y. Yu, X. Lin, and B. Zhang, Topologically protected refraction of robust kink states in valley photonic crystals, Nat. Phys. **14**, 140 (2018).

[34] J. Noh, S. Huang, K. P. Chen, and M. C. Rechtsman, Observation of Photonic Topological Valley Hall Edge States, Phys. Rev. Lett. **120**, 063902 (2018).

[35] C. Brendel, V. Peano, O. J. Painter, and F. Marquardt, Pseudomagnetic fields for sound at the nanoscale, Proc. Natl. Acad. Sci. U.S.A. **114**, E3390 (2017).

[36] J. Lu, C. Qiu, W. Deng, X. Huang, F. Li, F. Zhang, and Z. Liu, Valley Topological Phases in Bilayer Sonic Crystals, Phys. Rev. Lett. **120**, 116802 (2018).

[37] J. Lu, C. Qiu, M. Ke, and Z. Liu, Valley Vortex States in Sonic Crystals, Phys. Rev. Lett. **116**, 093901 (2016).

[38] J. Lu, C. Qiu, L. Ye, X. Fan, M. Ke, F. Zhang, and Z. Liu, Observation of topological valley transport of sound in sonic crystals, Nat. Phys. **13**, 369 (2017).

[39] M. Wang, L. P. Ye, J. Christensen, and Z. Y. Liu, Valley Physics in Non-Hermitian Artificial Acoustic Boron Nitride, Phys. Rev. Lett. **120**, 246601 (2018).

[40] B. Z. Xia, S. J. Zheng, T. T. Liu, J. R. Jiao, N. Chen, H. Q. Dai, D. J. Yu, and J. Liu, Observation of valley-like edge states of sound at a momentum away from the high-symmetry points, Phys. Rev. B **97**, 155127 (2018).

[41] M. Miniaci, R. K. Pal, R. Manna, and M. Ruzzene, Valley-based splitting of topologically protected helical waves in elastic plates, Phys. Rev. B **100**, 024304 (2019).

[42] R. Fleury, A. B. Khanikaev, and A. Alù, Floquet topological insulators for sound, Nat. Commun. **7**, 11744 (2016).

[43] H. Chen, H. Nassar, and G. L. Huang, A study of topological effects in 1D and 2D mechanical lattices, J. Mech. Phys. Solids **117**, 22 (2018).

[44] Z. L. Du, H. Chen, and G. L. Huang, Optimal quantum valley Hall insulators by rationally engineering Berry curvature and band structure, J. Mech. Phys. Solids **135**, 103784 (2020).

[45] K. Qian, D. J. Apigo, C. Prodan, Y. Barlas, and E. Prodan, Topology of the valley-Chern effect, Phys. Rev. B **98**, 155138 (2018).

[46] J. H. Ma, K. Sun, and S. Gonella, Valley Hall In-Plane Edge States as Building Blocks for Elastodynamic Logic Circuits, Phys. Rev. Appl. **12**, 044015 (2019).

[47] L. H. Wu and X. Hu, Scheme for Achieving a Topological Photonic Crystal by Using Dielectric Material, Phys. Rev. Lett. **114**, 223901 (2015).

[48] C. He, X. Xu, H. Ge, X. C. Sun, Y. B. Chen, M. H. Lu, X. P. Liu, and Y. F. Chen, Acoustic topological insulator and robust one-way sound transport, Nat. Phys. **12**, 1124 (2016).

[49] Z. W. Zhang, Q. Wei, Y. Cheng, T. Zhang, D. J. Wu, and X. J. Liu, Topological Creation of Acoustic Pseudospin Multipoles in a Flow-Free Symmetry-Broken Metamaterial Lattice, Phys. Rev. Lett. **118**, 084303 (2017).

[50] S. H. Mousavi, A. B. Khanikaev, and Z. Wang, Topologically protected elastic waves in phononic metamaterials, Nat. Commun. **6**, 8682 (2015).

[51] H. Chen, H. Nassar, A. N. Norris, G. K. Hu, and G. L. Huang, Elastic quantum spin Hall effect in kagome lattices, Phys. Rev. B **98**, 094302 (2018).

[52] W. A. Benalcazar, B. A. Bernevig, and T. L. Hughes, Quantized electric multipole insulators, Science **357**, 61 (2017).

[53] E. Khalaf, Higher-order topological insulators and superconductors protected by inversion symmetry, Phys. Rev. B **97**, 205136 (2018).

[54] M. Ezawa, Minimal models for Wannier-type higher-order topological insulators and phosphorene, Phys. Rev. B **98**, 045125 (2018).

[55] M. Ezawa, Higher-Order Topological Insulators and Semimetals on the Breathing Kagome and Pyrochlore Lattices, Phys. Rev. Lett. **120**, 026801 (2018).

[56] Z. W. Zhang, M. R. López, Y. Cheng, X. J. Liu, and J. Christensen, Non-Hermitian Sonic Second-Order Topological Insulator, Phys. Rev. Lett. **122**, 195501 (2019).

[57] J. Langbehn, Y. Peng, L. Trifunovic, F. von Oppen, and P. W. Brouwer, Reflection-Symmetric Second-Order Topological Insulators and Superconductors, Phys. Rev. Lett. **119**, 246401 (2017).

[58] H. R. Xue, Y. H. Yang, F. Gao, Y. D. Chong, and B. L. Zhang, Acoustic higher-order topological insulator on a Kagome lattice, Nat. Mater. **18**, 108 (2019).

[59] C. W. Peterson, W. A. Benalcazar, T. L. Hughes, and G. Bahl, A quantized microwave quadrupole insulator with topologically protected corner states, Nature **555**, 346 (2018).

[60] M. Serra-Garcia, V. Peri, R. Süsstrunk, O. R. Bilal, T. Larsen, L. G. Villanueva, and S. D. Huber, Observation of a phononic quadrupole topological insulator, Nature **555**, 346 (2018).

[61] X. Ni, M. Weiner, A. Alù, and A. B. Khanikaev, Observation of higher-order topological acoustic states protected by generalized chiral symmetry, Nat. Mater. **18**, 113 (2019).

[62] H. R. Xue, Y. H. Yang, G. G. Liu, F. Gao, Y. D. Chong, and B. L. Zhang, Realization of an Acoustic Third-Order Topological Insulator, Phys. Rev. Lett. **122**, 244301 (2019).

[63] H. Y. Fan, B. Z. Xia, L. Tong, S. J. Zheng, and D. J. Yu, Elastic Higher-Order Topological Insulator with Topologically Protected Corner States, Phys. Rev. Lett. **122**, 204301 (2019).